Global particle-in-cell simulations of Alfvénic modes

Alexey Mishchenko[*]

Max-Planck-Institut für Plasmaphysik,

EURATOM-Association, D-17491 Greifswald, Germany

Roman Hatzky

Rechenzentrum der Max-Planck-Gesellschaft

und des Max-Planck-Instituts für Plasmaphysik,

EURATOM-Association, D-85748 Garching, Germany

Axel Könies

Max-Planck-Institut für Plasmaphysik,

EURATOM-Association, D-17491 Greifswald, Germany

(Dated: March 11, 2009)

Abstract

Global linear gyrokinetic particle-in-cell (PIC) simulations of electromagnetic modes in pinch and tokamak geometries are reported. The Global Alfvén Eigenmode, the Mirror Alfvén Eigenmode, the Toroidal Alfvén Eigenmode and the Kinetic Ballooning Modes have been simulated. All plasma species have been treated kinetically (i.e. no hybrid fluid-kinetic or reduced-kinetic model has been applied). The main intention of the paper is to demonstrate that the global Alfvén modes can be treated with the gyrokinetic PIC method.

[*] alexey.mishchenko@ipp.mpg.de

I.   INTRODUCTION

Significant progress has been achieved in gyrokinetic turbulence simulation assuming electrostatic perturbations. However, in the presence of magnetic fluctuations, there exist new branches of modes, for example the Alfvénic Ion Temperature Gradient driven mode (AITG) (or Kinetic Ballooning Mode – KBM), the Toroidicity-induced Alfvén Eigenmode (TAE) that can play an important role for plasma stability and transport. Kinetic modifications to Magneto-Hydro-Dynamic (MHD) modes are important as well because its associated nonlinear effects can lead to a significant loss of fast particles. Another application for these modes is the so-called MHD spectroscopy, where the basic properties of the magnetic equilibrium (such as the safety factor profile) can be determined measuring the MHD activity. The destabilization of the shear Alfvén waves occurs as a result of a competition of the drive by fast particles and various damping mechanisms due to non-ideal (kinetic) effects such as electron and ion Landau damping, collisional damping, continuum damping, radiative damping, etc. A proper description of the various damping mechanisms is a key issue in determining stability criteria of energetic particle-driven Alfvén modes in burning plasma experiments. Still, the proper description of damping mechanisms is an issue of debate [1–6]. Furthermore, there are measurements of mode damping from the Mega-Ampere Spherical Tokamak [7, 8] and the Joint European Torus [9] to be expected.

The most rigorous first-principle approach to the kinetic theory of MHD modes is the global gyrokinetic description. Recently, a global gyrokinetic eigenvalue code [2, 3] has been developed. Being capable of capturing all kinetic effects in the linear regime, this approach is however difficult to extend for nonlinear problems. In contrast, the gyrokinetic particle-in-cell (PIC) method can be used both in linear and nonlinear regimes. In the past, electromagnetic PIC simulations have struggled with stringent numerical constraints associated with the so-called cancellation problem [10, 11]. This problem has been solved recently (see Refs. [10–14]). The key point to its solution is a careful balance between the adiabatic current computed with the markers and the so-called skin terms in Ampére's law discretized on the spatial grid (see Ref. [11] for details). In this paper, we employ the method of Ref. [14] to solve the cancellation problem.

The paper is organized as follows. In Sec. II, the basic equations and their discretization are presented. Sec. III describes the simulation of the Global Alfvén Eigenmode, Sec. IV dis-

cusses the simulation of the Kinetic Mirror Alfvén Eigenmode, while results for the Toroidal Alfvén Eigenmode are shown in Sec. V. Finally, before some concluding remarks (Sec. VII) the simulation of Kinetic Ballooning Modes is discussed in Sec. VI.

II. BASIC EQUATIONS AND NUMERICAL APPROACH

We use the linear two-dimensional δf PIC-code GYGLES. The code allows for electromagnetic perturbations and treats all particle species (ions and electrons) on the same footing (kinetically). In this section, we give a short description of the equations solved in the code. A detailed description can be found in Refs. [11–18].

The code solves the gyrokinetic Vlasov-Maxwell system of equations [19, 20]. The distribution function is split into the background part and the perturbation $f_s = F_{0s} + \delta f_s$ (the index $s = i, e$ is used for the particle species). The background distribution function is usually taken to be a Maxwellian. The perturbed distribution function δf_s is found from the linearized Vlasov equation:

$$\frac{\partial \delta f_s}{\partial t} + \dot{\mathbf{R}}^{(0)} \cdot \frac{\partial \delta f_s}{\partial \mathbf{R}} + \dot{v}_\parallel^{(0)} \frac{\partial \delta f_s}{\partial v_\parallel} = -\dot{\mathbf{R}}^{(1)} \cdot \frac{\partial F_{0s}}{\partial \mathbf{R}} - \dot{v}_\parallel^{(1)} \frac{\partial F_{0s}}{\partial v_\parallel}. \tag{1}$$

Here, $[\dot{\mathbf{R}}^{(0)}, \dot{v}_\parallel^{(0)}]$ correspond to the unperturbed gyro-center position and parallel velocity. $[\dot{\mathbf{R}}^{(1)}, \dot{v}_\parallel^{(1)}]$ are the perturbation of the particle trajectories proportional to the electromagnetic field fluctuations. The equations of motion are:

$$\dot{\mathbf{R}} = \left(v_\parallel - \frac{q}{m} \langle A_\parallel \rangle \right) \mathbf{b}^* + \frac{1}{qB_\parallel^*} \mathbf{b} \times \left[\mu \nabla B + q \left(\nabla \langle \phi \rangle - v_\parallel \nabla \langle A_\parallel \rangle \right) \right] \tag{2}$$

$$\dot{v}_\parallel = -\frac{1}{m} \left[\mu \nabla B + q \left(\nabla \langle \phi \rangle - v_\parallel \nabla \langle A_\parallel \rangle \right) \right] \cdot \mathbf{b}^* \tag{3}$$

with ϕ and $A_\parallel$ being the perturbed electrostatic and magnetic potentials, μ the magnetic moment, m the mass of the particle, $B_\parallel^* = \mathbf{b} \cdot \nabla \times \mathbf{A}^*$, $\mathbf{b}^* = \nabla \times \mathbf{A}^*/B_\parallel^*$, $\mathbf{A}^* = \mathbf{A} + (mv_\parallel/q)\mathbf{b}$ the so-called modified vector potential, $\mathbf{A}$ the magnetic potential corresponding to the equilibrium magnetic field $\mathbf{B} = \nabla \times \mathbf{A}$ and $\mathbf{b} = \mathbf{B}/B$ the unit vector in the direction of the equilibrium magnetic field. The gyro-averaged potentials are defined as usual:

$$\langle \phi \rangle = \oint \frac{d\theta}{2\pi} \phi(\mathbf{R} + \boldsymbol{\rho}), \quad \langle A_\parallel \rangle = \oint \frac{d\theta}{2\pi} A_\parallel(\mathbf{R} + \boldsymbol{\rho}), \tag{4}$$

where $\boldsymbol{\rho}$ is the gyro-radius of the particle and θ is the gyro-phase. The perturbed electrostatic and magnetic potentials are found self-consistently from the gyrokinetic quasi-neutrality

equation and parallel Ampére's law:

$$-\nabla \cdot \left(\frac{en_0}{T_i}\rho_i^2\nabla_\perp\phi\right) = (n_i - n_e) \ , \quad \left(\frac{\beta_i}{\rho_i^2} + \frac{\beta_e}{\rho_e^2} - \nabla_\perp^2\right)A_\| = \mu_0\left(j_{\|i} + j_{\|e}\right) \ , \qquad (5)$$

where $n_s = \int \mathrm{d}^6 Z \, F_s \, \delta(\mathbf{R} + \boldsymbol{\rho} - \mathbf{x})$ is the gyro-center density, $j_{\|s} = q_s \int \mathrm{d}^6 Z \, F_s \, v_\| \, \delta(\mathbf{R} + \boldsymbol{\rho} - \mathbf{x})$ is the gyro-center current, q_s is the charge of the particle, $\mathrm{d}^6 Z = B_\|^* \, \mathrm{d}\mathbf{R} \, \mathrm{d}v_\| \, \mathrm{d}\mu \, \mathrm{d}\theta$ is the phase-space volume, $\rho_s = \sqrt{m_s T_s}/(eB)$ is the thermal gyro-radius and $\beta_s = \mu_0 n_0 T_s / B_0^2$ is the plasma beta corresponding to a particular species. In practice, we modify the quasi-neutrality equation and Ampére's law to the following:

$$-C_\mathrm{q}\nabla \cdot \left(\frac{en_0}{T_i}\rho_i^2\nabla_\perp\phi\right) = (n_i - n_e) \ , \quad C_\mathrm{A}\left(\frac{\beta_i}{\rho_i^2} + \frac{\beta_e}{\rho_e^2}\right)A_\| - \nabla_\perp^2 A_\| = \mu_0\left(j_{\|i} + j_{\|e}\right) \ , \quad (6)$$

where the quantities C_q and C_A take into account the finite extent of the velocity-space domain which is limited to the sphere $v \le \kappa_\mathrm{v} v_\mathrm{th}$ (see Ref. [11] for details) in the simulations:

$$C_\mathrm{q} = \mathrm{erf}\left(\frac{\kappa_\mathrm{v}}{\sqrt{2}}\right) - \sqrt{\frac{2}{\pi}} \, \kappa_\mathrm{v} \, \exp\left(-\frac{\kappa_\mathrm{v}^2}{2}\right) \ ; \quad \mathrm{erf}(x) = \frac{2}{\sqrt{\pi}}\int_0^x e^{-t^2}\mathrm{d}t \qquad (7)$$

$$C_\mathrm{A} = \mathrm{erf}\left(\frac{\kappa_\mathrm{v}}{\sqrt{2}}\right) - \sqrt{\frac{2}{\pi}} \, \kappa_\mathrm{v}\left(1 + \frac{\kappa_\mathrm{v}^2}{3}\right)\exp\left(-\frac{\kappa_\mathrm{v}^2}{2}\right) \qquad (8)$$

The perturbed part of the distribution function is discretized with markers:

$$\delta f_s(\mathbf{R}, v_\|, \mu, t) = \sum_{\nu=1}^{N_p} w_{s\nu}(t)\delta(\mathbf{R} - \mathbf{R}_\nu)\delta(v_\| - v_{\nu\|})\delta(\mu - \mu_\nu) \ , \qquad (9)$$

where N_p is the number of markers, $(\mathbf{R}_\nu, v_{\nu\|}, \mu_\nu)$ are the marker phase space coordinates and $w_{s\nu}$ is the weight of a marker. The electrostatic and magnetic potentials are discretized with the finite-element method (Ritz-Galerkin scheme):

$$\phi(\mathbf{x}) = \sum_{l=1}^{N_s} \phi_l \Lambda_l(\mathbf{x}) \ , \quad A_\|(\mathbf{x}) = \sum_{l=1}^{N_s} a_l \Lambda_l(\mathbf{x}) \ , \qquad (10)$$

where $\Lambda_l(\mathbf{x})$ are the finite elements (tensor product of B splines [21, 22]), N_s is the total number of the finite elements, ϕ_l and a_l are the spline coefficients. A detailed description of the discretization procedure can be found in Refs. [11, 12, 14, 15, 17]. We apply the so-called phase factor transform [15] to all perturbed quantities in the code. The cancellation problem [10, 11] is solved using the iterative scheme No. 2 described in Ref. [14].

III. GLOBAL ALFVÉN EIGENMODE

The Global Alfvén Eigenmode (GAE) is basically an MHD mode [23, 24] with a frequency below the minimum of the Alfvén continuum branch with given mode numbers (m and n). This mode can be formed as a result of the presence of the equilibrium current density profile [24]. The GAE mode is known [23] to exhibit a spatial localization around the radial position $r = r_c$ where the Alfvén continuum has a minimum $\mathrm{d}\omega_A/\mathrm{d}r = 0$.

The simplest geometry where the GAE mode can be found is a screw pinch. We consider a screw pinch with the safety factor $q = 1.05 + 3.25s^2$ (the flux surface label $s = \sqrt{\psi/\psi_a}$, where ψ is the poloidal flux and ψ_a is the poloidal flux on the edge), the length of the pinch $L = 2\pi R_0$ (here $R_0 = 5.5$ m), the radius of the pinch $r_0 = 0.55$ m. We assume flat temperature profiles $T_i = T_e = 5$ keV and the profile of the plasma beta $\beta(\%) = 0.6(1 - s^2) + 0.045$.

To compute the background parallel current, we substitute the background magnetic field $\mathbf{B} = \nabla\psi \times \nabla\varphi + T(\psi)\nabla\varphi$ into Ampére's law. The resulting expression for the background parallel current density is $j_\parallel^{(0)} = (B/\mu_0)\,\mathrm{d}T/\mathrm{d}\psi$. Assuming that this current is carried by the electrons, one can write it as

$$j_\parallel^{(0)} = -e\int v_\parallel \mathrm{d}v_\parallel 2\pi v_\perp \mathrm{d}v_\perp F_{0e} = -en_0 u_e \ , \tag{11}$$

where u_e is the mean electron velocity and F_{0e} is the electron background distribution function. We choose it to be a shifted Maxwellian:

$$F_{0e} = n_0 \left(\frac{m_e}{2\pi T_e}\right)^{3/2} \exp\left[-\frac{m_e(v_\parallel - u_e)^2}{2T_e}\right]\exp\left[-\frac{m_e v_\perp^2}{2T_e}\right] \ . \tag{12}$$

Note that actually a Spitzer problem [25] must be solved to obtain the distribution function which then is not a shifted Maxwellian. However, detailed effects of the equilibrium are more important for other type of modes as e.g. the internal kink. Thus we leave it as a topic for further investigation.

The velocity shift in the Maxwell distribution function will affect the right-hand-side of the Vlasov equation, Eq. (1), but also Ampére's law has to be rewritten as follows:

$$\left(C_A - C_q \frac{u_e^2}{v_{\mathrm{the}}^2}\right)\frac{\omega_{\mathrm{pe}}^2}{c^2}A_\parallel - \nabla_\perp^2 A_\parallel = \mu_0\left(j_{\parallel i} + j_{\parallel e}\right) \ . \tag{13}$$

Drift kinetic electrons have been used to derive Eq. (13) and an unshifted Maxwellian has been assumed for the ion background distribution function. The simulation domain in the

velocity space is shifted for electrons so that $-\kappa_v v_{\text{the}} + u_e \leq v_\parallel \leq \kappa_v v_{\text{the}} + u_e$ (an appropriate "shifted initial loading" is employed).

In Fig. 1, the shear Alfvén spectrum from ideal MHD for the mode numbers ($m = 2$, $n = 1$) is plotted together with the simulation result. One can see that the frequency of the GAE mode resulting from the PIC simulations is close to that obtained with the three-dimensional linear MHD stability code CAS3D [26] and is indeed below the minimum of the continuum branch. Throughout the paper all MHD continua have been calculated using the CONTI code [27]. In Fig. 2, the electrostatic and magnetic potentials of the mode are shown. One sees that the gyrokinetic eigenmode structure is quite close to the ideal MHD result. As expected, the maximum of the eigenmode is close to the position of the minimum of the Alfvén continuum. In contrast to MHD, not only the frequency but also the collisionless damping rate of the GAE mode can be found within the gyrokinetic approach (note that the mode is marginally stable in ideal MHD). For the parameters used, $\omega = 5$ MHz and $\gamma = -24$ kHz have been obtained. The ratio between the damping rate and the frequency is $\gamma/\omega \approx 0.5\%$. The numerical parameters in our simulation are as follows: the number of ion markers $N_i = 500\,000$, the number of electron markers $N_e = 500\,000$, the number of radial B-splines $N_r = 64$, the number of B-splines in the parallel direction $N_z = 4$ and the time step $\Delta t = 10^{-8}$ s. In our simulations, we have employed the iterative approach of Ref. [14] to solve the cancellation problem [10, 11]. This gives us the capability to go beyond the first calculations (no plasma β) of a GAE mode within a PIC approach [28].

The computation of the GAE mode is an important step towards the global gyrokinetic simulation of so-called cascade modes in tokamaks (see Ref. [29] and the papers cited therein) which belong to the same type (associated with an extremum in the Alfvén continuum) as the Global Alfvén Eigenmodes [29]. Also note the importance of the GAE modes for the low-shear stellarators like Wendelstein-7X [28, 30].

IV. KINETIC MIRROR ALFVÉN EIGENMODE

In a cylindrical pinch, the branches of the shear Alfvén continuum belonging to different Fourier mode numbers can cross each other. In arbitrary geometry, the background magnetic field can be written as

$$B = \sum_{m,n} B_{mn}(s) \cos(m\theta - nN_{\text{per}}\varphi) \tag{14}$$

with the poloidal and toroidal angles (θ, φ), the poloidal and toroidal mode numbers (m, n), and the number of periods N_{per}. One can see that different mode numbers can couple with each other due to the geometry where correspondingly $B_{mn} \neq 0$. This coupling forms gaps in the crossing points, breaking the degeneracy of the Alfvén spectrum. It is known that global eigenmodes can exist inside such gaps [31]. One example of such a global mode is the Mirror Alfvén Eigenmode (MAE) which exists in the gap of the shear Alfvén continuum introduced by the "mirror harmonic" B_{01} of the background magnetic field. The radial position r_n of the MAE gap corresponding to the toroidal mode numbers n and $n + N_{\mathrm{per}}$ and to the poloidal mode number m can be found from the value of the rotational transform: $\iota(r_n) = (N_{\mathrm{per}}/2 + n)/m$.

Non-ideal effects such as finite gyro-radius effects or electron parallel dynamics replace the shear Alfvén continuum by a discrete spectrum of Kinetic Alfvén Waves (KAW) [32]. Two KAWs can interact in the vicinity of the gap leading to the formation of the quasi-steady states appearing as new global modes in the KAW spectrum [33]. Such a mode in the vicinity of the "mirror" gap is called the Kinetic Mirror Alfvén Eigenmode (KMAE) [34].

There are experimental data indicating that the MAE and KMAE modes have possibly been observed in stellarator experiments [35]. The mirror component of the equilibrium magnetic field is especially important for the optimized stellarators of the Wendelstein line [36]. A preliminary analysis of a stellarator reactor configuration has shown that the MAE and KMAE modes possibly cause the largest energy loss, being resonant with most energetic α-particles [37].

The simplest configuration where the mirror-type coupling can occur is the bumpy pinch. It is obtained setting all Fourier components of the magnetic field Eq. (14) except the mirror component B_{01} to zero so that $B = B_0[1 + c_0 \cos(N_{\mathrm{per}}\varphi)]$ with $B_0 = B_{00}$ and the bumpiness parameter $c_0 = B_{01}/B_{00}$. We consider a bumpy pinch with the parameters close to the stellarator Wendelstein 7-X [36]: the length of the pinch $L = 2\pi R_0$ with the large radius $R_0 = 5.5$ m, the minor radius $r_{\mathrm{a}} = 0.55$ m, the magnetic field on axis $B_0 = 2.5$ T, the number of the periods $N_{\mathrm{per}} = 5$ and the bumpiness $c_0 = 0.12$. The safety factor $q(s) = 0.0587s^3 - 0.2071s^2 + 0.0062s + 1.1762$ with $s = \sqrt{\psi/\psi_{\mathrm{a}}}$ the flux-surface label, ψ the magnetic poloidal flux and ψ_{a} the poloidal flux on the plasma edge. The ion end electron

densities are given by the expression (here $a = i, e$):

$$n_a(s) = n_0(1.0011 - 0.04230s + 0.6511s^2 - 5.5094s^3 + 27.496s^4 - \qquad (15)$$
$$87.165s^5 + 177.74s^6 - 228.92s^7 + 172.29s^8 - 65.518s^9 + 8.8187s^{10}) \,.$$

The ion and electron temperatures are constant $T_i(s) = T_{i0}$ and $T_e(s) = T_{e0}$. The parameters chosen are $n_0 = 10^{19}$ m^{-3}, $T_{i0} = T_{e0} = 5$ keV (such parameters correspond to $\beta \approx 0.67\%$ in the position of the gap). The numerical parameters in our simulations are as follows: the number of ion markers $N_i = 1\,000\,000$, the number of electron markers $N_e = 4\,000\,000$, the number of radial B-splines $N_r = 64$, the number of B-splines in the parallel direction $N_z = 8$, the time step $\Delta t = 10^{-8}$ s.

We present the results of our simulations in Figs. 3-5. In Fig. 3, the corresponding part of the Alfvén spectrum is plotted. One can see that the frequency of the simulated global mode $\omega = 6$ MHz lies slightly above the gap in the continuum which corresponds to the Kinetic Mirror Alfvén Eigenmode (KMAE) [34]. In Fig. 4, the eigenmode structure of the electrostatic potential and the magnetic potential is shown. One can see, as expected, that the eigenmode is located around the position of the "mirror" gap (cf. Fig. 3) $s = 0.5$ in the shear Alfvén spectrum. Both the mode width and the mode frequency agree well with the reduced-kinetic approach proposed in Ref. [34]. However, in our simulations we clearly see an even eigenmode (the electrostatic potential corresponding to the coupling Fourier modes has the same sign) whereas a reduced-kinetic computation similar to Ref. [34] suggests that the eigenmode is odd (the coupling Fourier components have opposite sign). A detailed in-depth comparison of the reduced-kinetic model [34] and the gyrokinetic theory is needed to understand this rather subtle discrepancy. Such a study is, however, beyond the scope of the present paper whose main objective is to report the results of our PIC simulations. In Fig. 5, the time evolution of the electrostatic potential and the magnetic potential is plotted. One can see that the Fourier modes with the toroidal mode numbers differing in N_{per} ($n = -14$ and $n = -9$) couple with each other (they have the same phase and similar amplitude) indicating that we have found indeed the KMAE mode. This mode is damped. The damping rate is $\gamma = -40.12$ kHz so that $\gamma/\omega \approx 0.67\%$.

Continuing the simulation for a longer time, we have found that there are other damped components in the resulting time trace in addition to the dominant eigenmode described above. These additional components (e.g. KMAEs with several knots in their radial struc-

8

ture, see Ref. [34]) form a discrete spectrum in the vicinity of the mirror-induced gap in the shear Alfvén spectrum. We have observed similarly complex time traces in the vicinity of the toroidicity-induced gap. This issue will be discussed in detail in the next paragraph.

V.   TOROIDAL ALFVÉN EIGENMODE

A more prominent example of the global gap modes in the shear Alfvén spectrum is the Toroidal Alfvén Eigenmode (TAE). This is a global mode inside the gap induced by the "toroidiciy" harmonic B_{10} in the Fourier expansion of the background magnetic field Eq. (14). The radial position r_m of the gap corresponding to the poloidal mode numbers m and $m+1$ can be found from the value of the safety factor: $q(r_m) = (1/2 + m)/n$ with n the toroidal mode number. Analogously to the case of the mirror-induced gap, an interaction between two KAWs in the vicinity of the toroidicity-induced gap can lead to a formation of meta-stable states appearing as a new global kinetic mode in the shear Alfvén spectrum, the so-called Kinetic Toroidal Alfvén Eigenmode (KTAEs), see Ref. [1, 2, 33].

We consider a large-aspect-ratio circular cross-section tokamak with the major radius $R_0 = 10$ m, the minor radius $r_a = 1$ m, the magnetic field on the axis $B_0 = 0.95$ T, the safety factor $q(r) = 1.6 + 0.6(r/r_a)^2$ with r the small radius. The ion and electron temperature and density profiles are taken to be constant with $T_i = T_e = 3.8$ keV and $n_0 = 2 \times 10^{18}$ m^{-3} [these parameters correspond to $\beta = 2\mu_0 n_0 (T_i + T_e)/B^2 \approx 0.7\%$]. We use flat profiles in order to exclude the influence of diamagnetic effects on the TAE mode (their role will be studied elsewhere).

In the PIC method, one solves the gyrokinetic Vlasov-Maxwell system as an initial-value problem. We choose as initial condition the perturbation of the electron distribution function with the toroidal mode number $n = -2$ and the poloidal spectrum including two harmonics with $m = 3$ and $m = 4$. For the safety factor used, the gap in the shear Alfvén spectrum resulting from the coupling of these poloidal harmonics corresponds to $q_m = 1.75$ and appears at the radial position $s_m = 0.5$ (here, $s = \sqrt{\psi/\psi_a}$ is the normalized poloidal flux). We choose the initial electron perturbation to be radially localized around the position of the gap s_m. The initial velocity space dependency of the electron distribution function is chosen to be Maxwellian. The initial ion distribution function is chosen to be zero.

In Fig. 6, the solution of the initial-value gyrokinetic problem is plotted (both the elec-

trostatic and magnetic potentials). In this simulation, the numerical parameters are the same as in Table III. One can see a damped signal with a characteristic beating structure indicating that there are several eigenmodes mixed in the time trace. Note that these eigenmodes have close frequencies (the beating frequency is small) which makes the eigenmode separation technically difficult: one needs long runs but the runtime is limited for damped modes because at some point the physically relevant damped signal becomes comparable with the numerical noise. This in contrast with the eigenvalue approach Ref. [2] where a particular eigenmode is selected naturally.

One can estimate the frequencies of the modal components using the Fourier analysis. For the signal shown, the Fourier component with the largest amplitude is that with the frequency $\omega = 0.417$ MHz (see Fig. 7). In addition, the Fourier component with the frequency $\omega = 0.44$ MHz can also be clearly seen. Both dominant frequencies are inside the toroidicity-induced gap (see Fig. 9) indicating that these eigenmodes belong to the TAE family. Indeed, in Fig. 8 one can clearly see two coupling poloidal harmonics with the poloidal mode numbers $m = 3$ and $m = 4$ (the much smaller sidebands can be seen as well). Note that the dominant poloidal harmonics of the electrostatic potential coincide in their phase whereas they have opposite phases for the magnetic potential. Formally, this can be seen combining the local condition for the appearance of the gap in the shear Alfvén spectrum $k_{\parallel m} + k_{\parallel m+1} = 0$ with the ideal MHD property $E_\parallel = -\nabla_\parallel \phi - \partial A_\parallel / \partial t \approx 0$ where $k_\parallel$ is the parallel wave number and $E_\parallel$ is the parallel electric field.

In the ideal MHD calculations (using an eigenvalue code) we have found two TAE modes: one with the frequency at the lower end of the gap and another one with the frequency at the upper end (see Fig. 9). One sees that the frequencies found with the gyrokinetic PIC code are shifted slightly inside the gap comparing with the ideal MHD frequencies. This can be caused by several reasons. First of all, the gyrokinetic model includes all kinetic effects such as the finite electron conductivity, finite ion compressibility, Finite Larmor Radius effects etc. All these effects are absent in the ideal MHD model. Another possible reason for the differences between the ideal MHD and the gyrokinetic frequencies may be related to the treatment of the plasma background. In the PIC simulation, we take an analytic large-aspect-ratio expressions for the background magnetic field whereas the ideal MHD code uses numerical equilibria (produced by the VMEC code [38]). Also, the ideal MHD code assumes the plasma density profile to decrease at the edge whereas the flat density profile is used for

the PIC simulation.

In Fig. 10, the eigenmode structure of the ideal MHD TAE mode with the frequency at the lower end of the gap is compared with the radial structure resulting from the gyrokinetic PIC simulation. The gyrokinetic radial structure has been taken at some particular point of time and represents a typical pattern seen in the simulations. This pattern can be clearly seen, for example, near the maximums of the TAE oscillations (see Fig. 8). At the points where the signal crosses zero, one sees usually more complicated structures dominated by the sidebands. Both the gyrokinetic radial pattern and the ideal MHD eigenmode are localized around the radial position r_m of the gap. In Fig. 10, one can see that the gyrokinetic radial pattern resembles the ideal MHD eigenmode reasonably well, especially taking into account that the gyrokinetic signal is actually a mixture of more than one eigenmode. Also, the differences in the gyrokinetic and ideal MHD models as well as the differences in the treatment of the plasma background mentioned above may have influenced the result.

The ideal MHD results have been calculated using a reduced MHD model which is the limiting case of the kinetic theory applied here. Within the complete MHD model (such as used in CAS3D [26]) the TAE mode properties can be modified by finite β effects (the mode structure becomes more localized in the radial direction and the mode frequency is closer to the continuum). A detailed in-depth comparison of the gyrokinetic simulations in the MHD parameter range with the different formulations of the ideal MHD theory remains an important task for future research.

Note that the Fourier analysis is not really accurate for the damped sine waves (and can not be used to determine the damping rates). Instead, we employ Prony's method [39]. This method assumes that the signal can be expressed as a sum of complex exponents:

$$\phi(t) = \sum_{k=1}^{N} C_k \exp(\lambda_k t) \ , \ \ \lambda_k = i\omega_k + \gamma_k \ . \tag{16}$$

Being an extension of the Fourier analysis, Prony's method allows to estimate simultaneously the damping rate, the frequency and the complex amplitude of the modes contributing to the PIC solution of the initial-value gyrokinetic problem.

In Tables I, II and III, the amplitudes (absolute values), frequencies and damping rates obtained with Prony's method [see Eq. (16)] are shown for simulations using different particle and grid resolutions. Table I corresponds to a simulation with $N_i = 1\,800\,000$ ion markers, $N_e = 7\,200\,000$ electron markers, $N_r = 48$ radial B-splines, $N_z = 32$ B-splines in the toroidal

11

direction and the time step $\Delta t = 10^{-8}$ s. Table II has been obtained in a simulation with $N_i = 2\,000\,000$, $N_e = 8\,000\,000$, $N_r = 80$ and other numerical parameters the same as in Table I. Finally, Table III results from a simulation with $N_i = 4\,000\,000$, $N_e = 16\,000\,000$, $N_r = 80$ and other numerical parameters the same as in Table I. One sees that, in addition to the eigenmodes found using the Fourier analysis, eigenmodes with considerably larger damping rates are also present in the signal (possibly, KTAE modes). The relative contribution of a particular eigenmodes to the signal appears to depend on the particle and grid resolution. One can see that the dominant frequencies found with the Fourier transform correspond to the Prony's modal components with the smallest damping rates. These contributions are present at all resolutions. The relative deviation of the dominant frequencies over the simulations is less than 1%. The damping rates show somewhat larger relative deviations but this is due to the much smaller absolute values of the damping rates compared to the frequencies. One sees that our simulations have converged both in terms of the particle and grid resolution.

In conclusion, the existence of several eigenmodes with comparable frequencies and damping rates in the vicinity of the toroidicity-induced gap in the shear Alfvén spectrum is not something unusual. In fact, this is a typical situation [31]. In this paper, we have seen that advanced methods, such as Prony's method or its refinements, can be used to separate the eigenmodes mixed in the signal resulting from the initial-value PIC simulations.

VI. KINETIC BALLOONING MODE

At a critical value of the plasma pressure, a new branch of unstable electromagnetic modes can be excited [40], the so-called Kinetic Ballooning Modes (KBMs) or Alfvén Ion Temperature Gradient driven modes (AITG). In Ref. [41], it has been shown that the low-frequency part of the Alfvén continuum can become unstable in the presence of the ion temperature gradient. The AITG modes are drift-Alfvén eigenmodes, destabilized by the free energy of the thermal particles in the presence of the pressure gradient, resulting from the discretization of the unstable continuum due to non-ideal effects (e.g. Finite Larmor Radius effects). These instabilities may have significant implications for both energetic and thermal particle transport.

We consider a circular cross-section tokamak with the major radius $R_0 = 2.0$ m, the minor

radius $r_a = 0.5$ m, the safety factor $q(\rho) = 1.25 + 0.67\rho^2 + 2.38\rho^3 - 0.06\rho^4$ where $\rho = r/r_a$, r is the small radius. The temperature profiles $T_i(\rho) = T_e(\rho) = T_0 \exp\{-0.5\tanh[(\rho - 0.6)/0.2]\}$ with the temperature on the axis $T_0 = 7.5$ keV. The density profile is defined as $n_0(\rho) = n_a \exp\{-0.44\tanh[(\rho - 0.6)/0.35]\}$ with the density on the axis n_a chosen appropriately in order to obtain the β-value needed. We choose the toroidal mode number $n = 7$ and the poloidal mode numbers $8 \leq m \leq 20$. Results of our simulations are presented in Figs. 11 and 12. In Fig. 11, the frequency and the growth rate of the instability is plotted. One can see how the electrostatic mode (here, the Trapped Electron Mode coexisting with the Ion Temperature Gradient driven mode) is replaced by the KBM instability when β is large enough (recall that the time evolution particle-in-cell approach delivers the most unstable mode in the spectrum). In Fig. 12, the spatial structure of the electrostatic and the magnetic potentials is shown in the tokamak cross-section. One can see that both potentials have ballooning structure. The numerical parameters in our simulations are as follows: the number of the ion markers $N_i = 1\,000\,000$, the number of the electron markers $N_e = 4\,000\,000$, the number of radial B-splines $N_r = 64$, the number of B-splines in the toroidal direction $N_z = 32$, the time step $\Delta t = 5 \times 10^{-9}$ s.

VII. CONCLUSIONS

In this paper, we have presented global gyrokinetic PIC simulations of the Global Alfvén Eigenmode, Kinetic Mirror Alfvén Eigenmode, Toroidal Alfvén Eigenmode, and the Kinetic Ballooning Mode. The key numerical component of our simulations is the solution of the cancellation problem [10, 11] using the iterative approach of Ref. [14]. This allows to keep the number of markers in the same range as in comparable electrostatic PIC simulations. The main result of our paper is to demonstrate that global Alfvén modes can be treated in tokamak and pinch geometries in a unified manner with the gyrokinetic PIC method. Up to now, the kinetic properties of the global Alfvén modes in a tokamak geometry have been approached using reduced-kinetic [1], hybrid fluid-kinetic [42] or gyrokinetic-eigenvalue approaches [2]. The drawback of the reduced-kinetic and hybrid fluid-kinetic approaches is that they can not guarantee to include all relevant physical mechanisms. The gyrokinetic eigenvalue approach being capable to capture all physics is limited to linear problems only. Being a first-principle non-perturbative approach, the gyrokinetic PIC simulations can re-

cover all kinetic effects, too. For example, in this paper we have seen that such purely kinetic phenomena as the intrinsic damping of the global Alfvén eigenmodes due to background plasma and formation of kinetic global Alfvén modes in the continuum part of the spectrum (e.g. the Kinetic Mirror Alfvén eigenmode in Sec. IV) are present in the gyrokinetic PIC simulations. Recovering such kinetic properties of the global Alfvén modes with the gyrokinetic PIC method validates this approach as a reliable tool for future research in the MHD parameter regime. This validation appears to be especially important in the light of the difficulties which the electromagnetic PIC simulations have had for a long time [43–45] and which have been resolved only recently [10, 11, 14].

In contrast with the eigenvalue approach, the PIC method can be easily extended to nonlinear regimes. The linear simulations presented in this paper are an important step towards the global nonlinear gyrokinetic treatment of electromagnetic modes in tokamak geometry (both electromagnetic turbulence and nonlinear dynamics of kinetic MHD modes destabilized by the fast particles). The PIC simulation of the kinetic effects caused by the fast particles will be the focus of our future work.

[1] G. Y. Fu, H. L. Berk, and A. Pletzer, Phys. Plasmas **12**, 082505 (2005).

[2] P. Lauber, S. Günter, and S. D. Pinches, Phys. Plasmas **12**, 122501 (2005).

[3] P. Lauber, S. Günter, A. Könies, and S. D. Pinches, J. Comp. Phys. **226**, 447 (2007).

[4] A. Jaun, A. Fasoli, and W. Heidbrink, Phys. Plasmas **5**, 2952 (1998).

[5] A. Fasoli, A. Jaun, and D. Testa, Phys. Lett. A **265**, 288 (2000).

[6] A. Fasoli, C. Gormenzano, H. L. Berk, B. Breizman, S. Briguglio, D. S. Darrow, N. Gorelenkov,

W. W. Heidbrink, A. Jaun, S. V. Konovalov, R. Nazikian, J.-M. Noterdaeme, S. Sharapov, K. Shinohara, D. Testa, K. Tobita, Y. Todo, G. Vlad, and F. Zonca, Nucl. Fusion **47**, S264 (2007).

[7] B. Lloyd, R. J. Akers, F. Alladio, Y. Andrew, L. C. Appel, D. Applegate, K. B. Axon, N. Ben Ayed, C. Bunting, R. J. Buttery, P. G. Carolan, I. Chapman, D. Ciric, J. W. Connor, N. J. Conway, M. Cox, G. F. Counsell, G. Cunningham, A. Darke, E. Delchambre, R. O. Dendy, J. Dowling, B. Dudson, M. Dunstan, A. R. Field, A. Foster, S. Gee, L. Garzotti, M. P. Gryaznevich, A. Gurchenko, E. Gusakov, N. C. Hawkes, P. Helander, T. C. Hender, B. Hnat, D. F. Howell, N. Joiner, D. Keeling, A. Kirk, B. Koch, M. Kuldkepp, S. Lisgo, F. Lott, G. P. Maddison, R. Maingi, A. Mancuso, S. J. Manhood, R. Martin, G. J. McArdle, J. McCone, H. Meyer, P. Micozzi, A. W. Morris, D. G. Muir, M. Nelson, M. R. O'Brien, A. Patel, S. Pinches, J. Preinhaelter, M. N. Price, E. Rachlew, C. M. Roach, V. Rozhansky, S. Saarelma, A. Saveliev, R. Scannell, S. E. Sharapov, V. Shevchenko, S. Shibaev, K. Stammers, J. Storrs, A. Surkov, A. Sykes, S. Tallents, D. Taylor, N. Thomas-Davies, M. R. Turnyanskiy, J. Urban, M. Valovic, R. G. L. Vann, F. Volpe, G. Voss, M. J. Walsh, S. E. V. Warder, R. Watkins, H. R. Wilson, M. Wisse, and the MAST and NBI teams, Nucl. Fusion **47**, S658 (2007).

[8] A. Sykes, J.-W. Ahn, R. Akers, E. Arends, P. G. Carolan, G. F. Counsell, S. J. Fielding, M. Gryaznevich, R. Martin, M. Price, C. Roach, V. Shevchenko, M. Tournianski, M. Valovic, M. J. Walsh, and H. R. Wilson, Phys. Plasmas **8**, 2101 (2001).

[9] P. H. Rebut and B. E. Keen, Fusion Technol. **11**, 13 (1987).

[10] Y. Chen and S. Parker, J. Comp. Phys **189**, 463 (2003).

[11] A. Mishchenko, R. Hatzky, and A. Könies, Phys. Plasmas **11**, 5480 (2004).

[12] A. Mishchenko, A. Könies, and R. Hatzky, Proceedings of the Joint Varenna-Lausanne International Workshop, Varenna, 2004, edited by J. W. Connor, O. Sauter, and E. Sindoni (Società Italiana di Fisica, Bologna, 2004), p. 315.

[13] R. Hatzky, A. Könies, and A. Mishchenko, Proceedings of the Joint Varenna-Lausanne International Workshop, Varenna, 2004, edited by J. W. Connor, O. Sauter, and E. Sindoni (Società Italiana di Fisica, Bologna, 2004), p. 13.

[14] R. Hatzky, A. Könies, and A. Mishchenko, J. Comp. Phys. **225**, 568 (2007).

[15] M. Fivaz, S. Brunner, G. de Ridder, O. Sauter, T. M. Tran, J. Vaclavik, L. Villard, and K. Appert, Comp. Phys. Commun. **111**, 27 (1998).

[16] S. Sorge and R. Hatzky, Plasma Phys. Control. Fusion **44**, 2471 (2002).

[17] A. Mishchenko, A. Könies, and R. Hatzky, Phys. Plasmas **12**, 062305 (2005).

[18] A. Mishchenko, R. Hatzky, and A. Könies, Proceedings of the Joint Varenna-Lausanne International Workshop, Varenna, 2004, edited by J. W. Connor, O. Sauter, and E. Sindoni (AIP Conference Proceedings, New York, 2006), Vol. 871, p. 394.

[19] T. S. Hahm, Phys. Fluids **31**, 2670 (1988).

[20] T. S. Hahm, W. W. Lee, and A. J. Brizard, Phys. Fluids **31**, 1940 (1988).

[21] C. de Boor, *A Practical Guide to Splines* (Springer-Verlag, New York, 1978).

[22] K. Höllig, *Finite Element Methods with B-Splines* (Society for Industrial and Applied Mathematics, Philadelphia, 2003).

[23] K. Appert, G. Gruber, F. Troyon, and J. Vaclavik, Plasma Phys. Controlled Fusion **24**, 1147 (1982).

[24] Y. M. Li, S. M. Mahajan, and D. W. Ross, Phys. Fluids **30**, 1466 (1987).

[25] P. Helander and D. J. Sigmar, *Collisional Transport in Magnetized Plasmas* (Cambridge University Press, Cambridge, 2002).

[26] C. Nührenberg, Phys. Plasmas **6**, 137 (1999).

[27] A. Könies, IAEA Technical Meeting on Innovative Concepts and Theory of Stellarators (2003).

[28] D. Eremin, Proceedings of the Joint Varenna-Lausanne International Workshop, Varenna, 2004, edited by J. W. Connor, O. Sauter, and E. Sindoni (AIP Conference Proceedings, New York, 2006), Vol. 871, p. 312.

[29] G. Y. Fu and H. L. Berk, Phys. Plasmas **13**, 052502 (2006).

[30] Z. N. Andrushchenko, O. K. Cheremnykh, and J. W. Edenstrasser, Phys. Plasmas **6**, 2462 (1999).

[31] C. Z. Cheng and M. S. Chance, Phys. Fluids **29**, 3695 (1986).

[32] S. M. Mahajan, Phys. Fluids **27**, 2238 (1984).

[33] R. R. Mett and S. M. Mahajan, Phys. Fluids B **4**, 2885 (1992).

[34] O. P. Fesenyuk, Ya. I. Kolesnichenko, V. Lutsenko, H. Wobig, and Yu. Yakovenko, Plasma Phys. Controlled Fusion **46**, 89 (2004).

[35] V. Lutsenko, Ya. I. Kolesnichenko, A. Weller, A. Werner, H. Wobig, Yu. Yakovenko, and O. Fesenyuk, in *Proc. 19th Int. Conf. on Fusion Energy* (IAEA-CN-94-TH/P3-16, Lyon, 2002).

[36] G. Grieger, C. D. Beidler, H. Maassberg, E. Harmeyer, F. Herrnegger, J. Junker, J. Kisslinger,

W. Lotz, P. Merkel, J. Nührenberg, F. Rau, J. Sapper, A. Schlüter, F. Sardei, and H. Wobig, in *Proc. of the 13th International Conference on Plasma Physics and Controlled Nuclear Fusion Research* (International Atomic Energy Agency, Vienna, 1991), Vol. 3, p. 525.

[37] Ya. I. Kolesnichenko, V. Lutsenko, H. Wobig, and Yu. Yakovenko, in *Scientific Papers of the Institute for Nuclear Research* (Institute for Nuclear Research, Kyiv, 2001).

[38] S. P. Hirshman, W. I. van Rij, and P. Merkel, Comp. Phys. Commun. **43**, 143 (1986).

[39] J. F. Hauer, C. J. Demeure, and L. L. Scharf, IEEE Transactions on Power Systems **5**, 80 (1990).

[40] F. Zonca, L. Chen, J. Q. Dong, and R. Santoro, Phys. Plasmas **6**, 1917 (1999).

[41] F. Zonca, L. Chen, and R. Santoro, Plasma Phys. Controlled Fusion **38**, 2011 (1996).

[42] Y. Nishimura, Z. Lin, and W. X. Wang, Phys. Plasmas **14**, 042504 (2007).

[43] J. V. W. Reynders, Ph.D. thesis, Princeton University, 1992.

[44] J. C. Cummings, Ph.D. thesis, Princeton University, 1995.

[45] Y. Chen and S. Parker, Phys. Plasmas **8**, 2095 (2001).
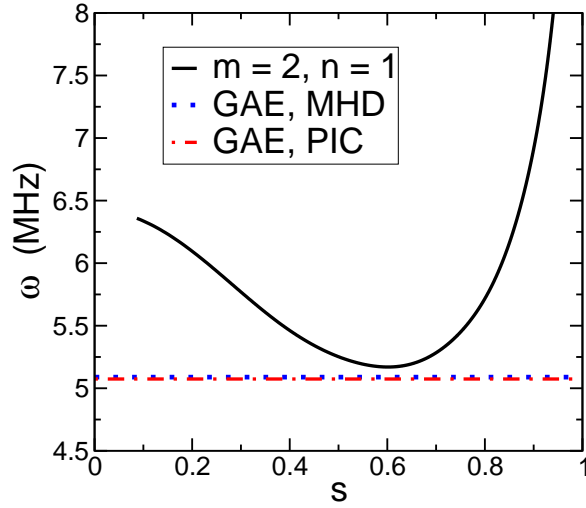
FIG. 1: (Color online): The shear Alfvén spectrum in a screw pinch. The GAE mode frequency resulting from the PIC simulation is compared with the MHD result. The solid line corresponds to the continuum branch with the poloidal mode number $m = 2$ and the toroidal mode number $n = 1$.
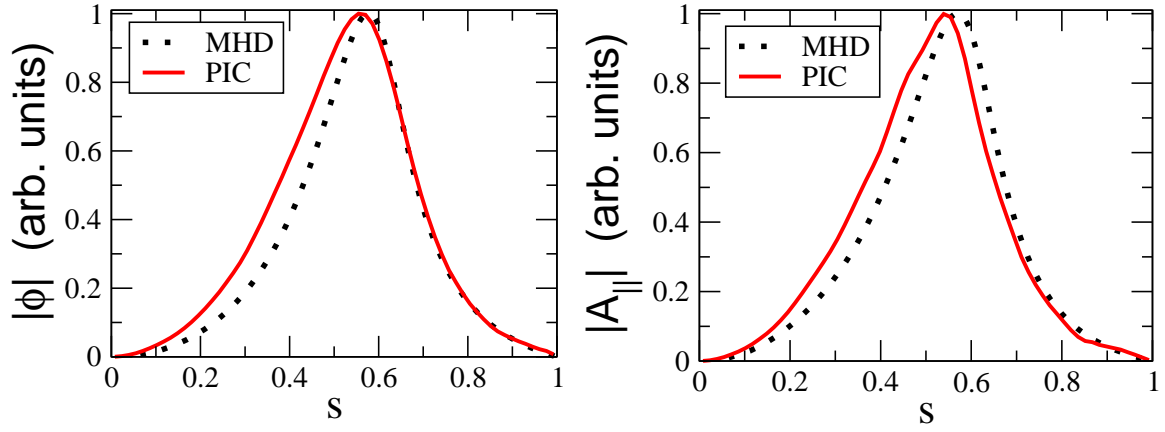
FIG. 2: (Color online): The eigenmode structure (the electrostatic and magnetic potentials in arbitrary units) of the GAE mode in screw pinch geometry. The PIC simulation result is compared vs. the MHD result.
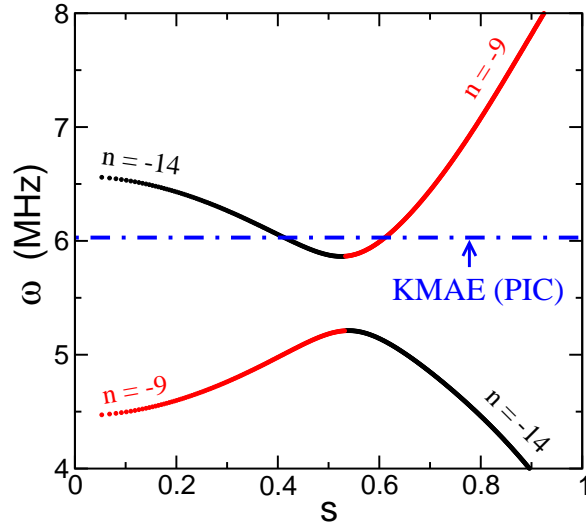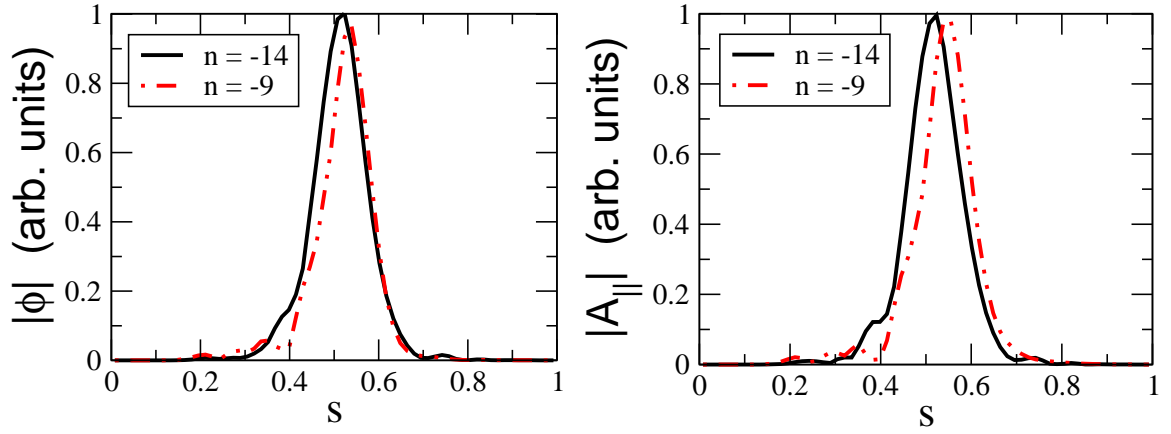
FIG. 3: (Color online): The shear Alfvén spectrum in a bumpy pinch. The KMAE mode frequency resulting from the PIC simulations is plotted vs. the continuum branches corresponding to the coupling modes with the toroidal mode numbers $n = -14$ and $n = -9$. The poloidal mode number is $m = 13$.

FIG. 4: (Color online): The eigenmode structure (the electrostatic and magnetic potentials in arbitrary units) of the KMAE mode in bumpy pinch geometry. One sees two coupling modes with the toroidal mode numbers $n = -14$ and $n = -9$. The poloidal mode number is $m = 13$.
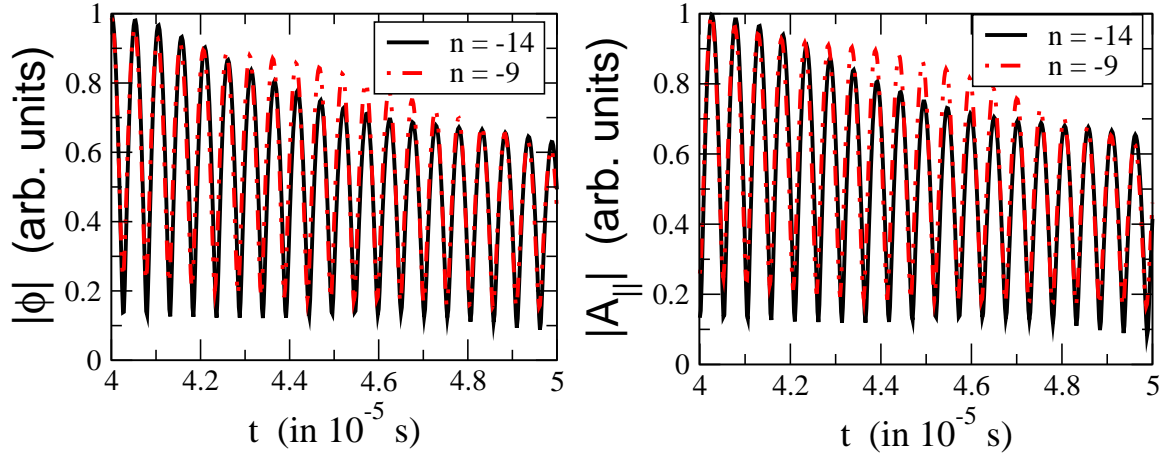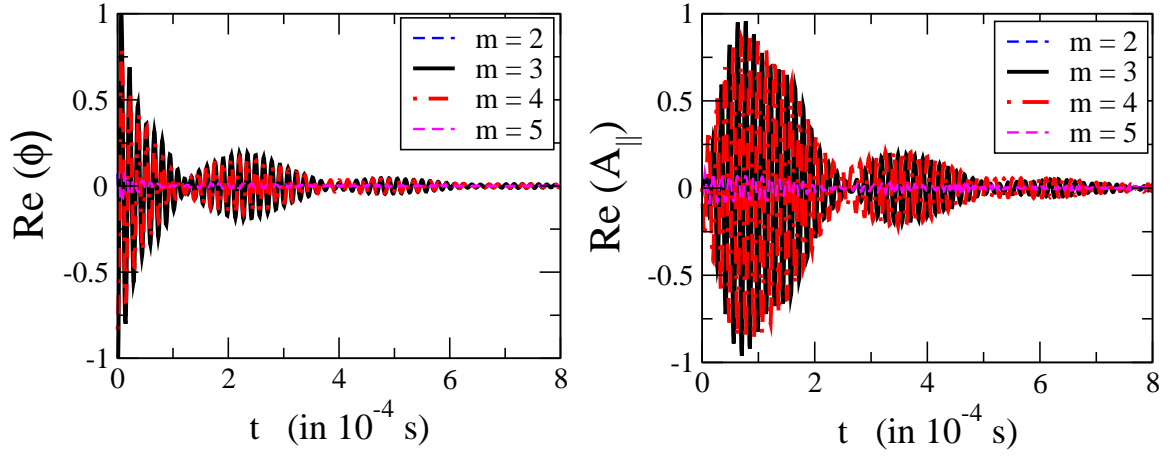
FIG. 5: (Color online): Time evolution of the electrostatic and magnetic potentials (arbitrary units). The KMAE mode in bumpy pinch geometry. One sees that the modes with the toroidal mode numbers $n = -14$ and $n = -9$ couple with each other. The poloidal mode number is $m = 13$.

FIG. 6: (Color online): Time evolution of the electrostatic and magnetic potentials (arbitrary units). The TAE mode in a tokamak with the coupling poloidal mode numbers $m = 3$ and $m = 4$. A beating structure indicates that more than just one eigenmode is present in the signal.
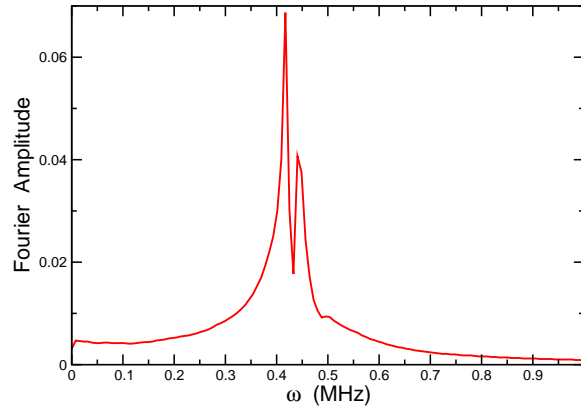
FIG. 7: (Color online): The Fourier spectrum of the signal Fig. 6. There are two dominant frequencies present in the signal which explains the beating seen on Fig. 6.
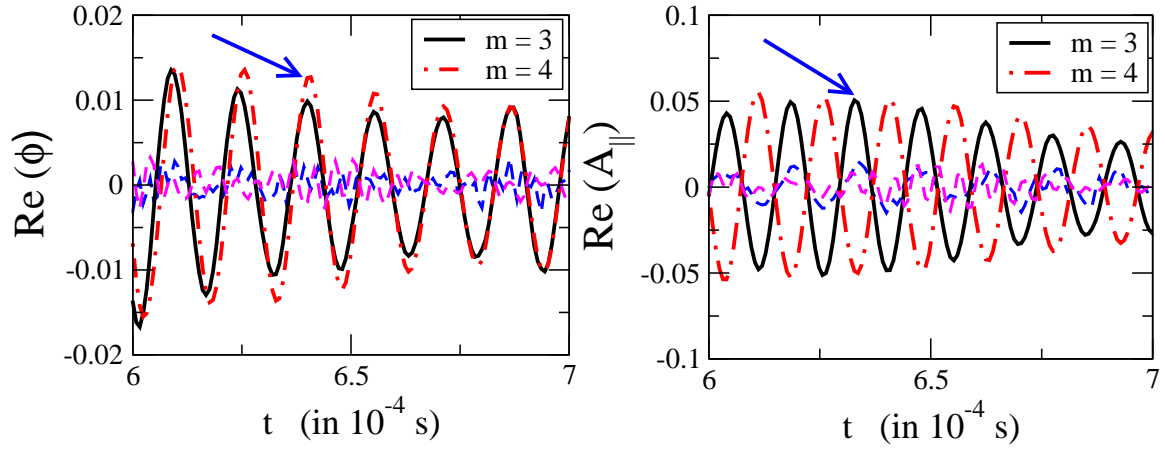
FIG. 8: (Color online): Zoom of Fig. 6. One sees that the coupling poloidal harmonics are very well correlated with each other. The much smaller sidebands are plotted as well. The arrows show a typical point in time at which the radial pattern (Fig. 10) can be clearly seen.
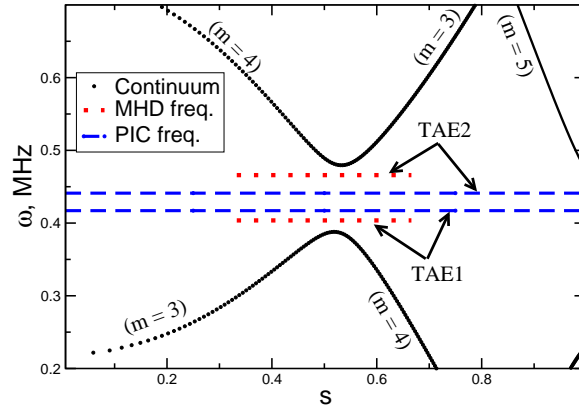
FIG. 9: (Color online): The shear Alfvén spectrum in a tokamak (for parameters see the main text). The dominant frequencies resulting from the PIC simulations are compared with the eigen-frequencies of the TAE modes obtained with the ideal MHD eigenvalue code. The continuum branches are plotted as well.
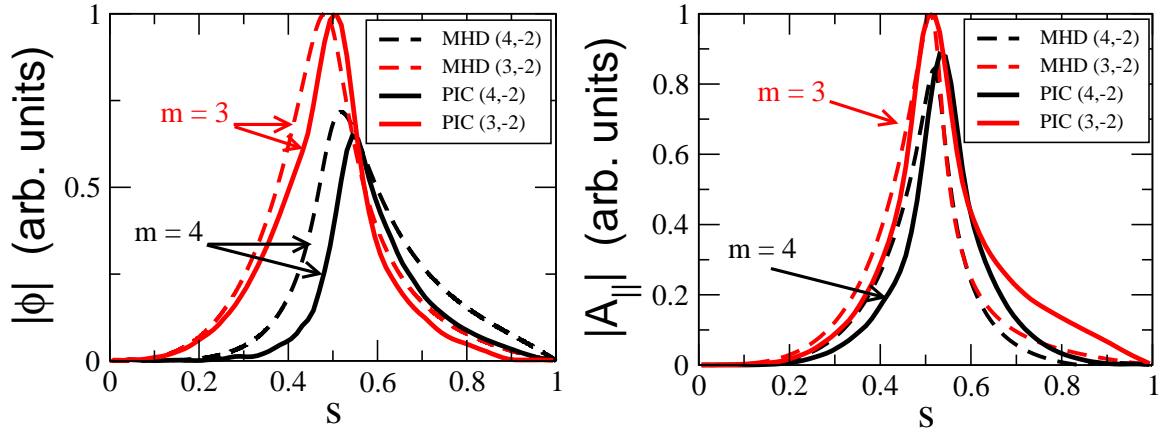
FIG. 10: (Color online): The radial pattern resulting from the PIC simulation (the electrostatic and magnetic potentials in arbitrary units) is compared with the ideal TAE (the mode at the lower end of the gap, see Fig. 9). The gyrokinetic radial pattern is taken at the point of time indicated with arrows in Fig. 8.
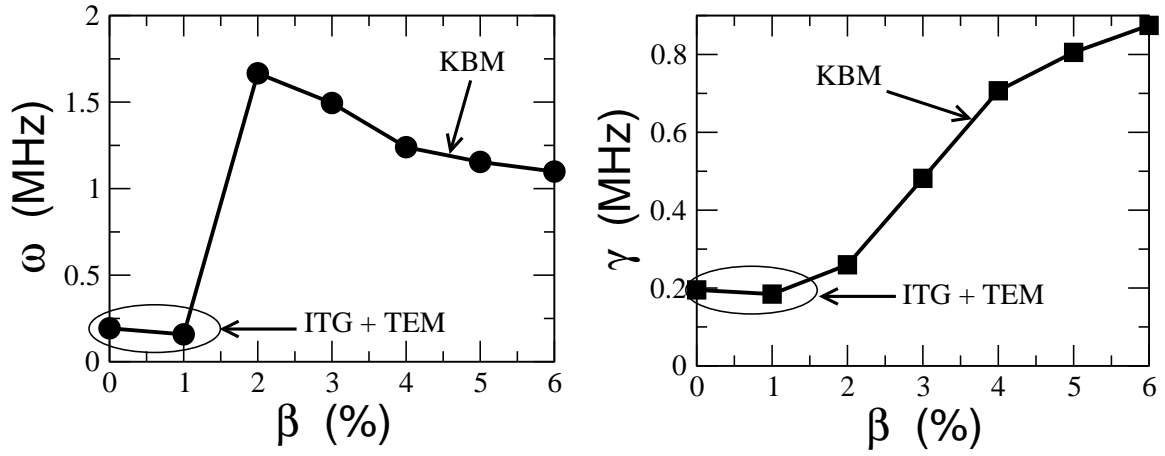
FIG. 11: The frequency and the growth rate of the ITG+TEM (small β) and KBM (larger β) instabilities in tokamak geometry.
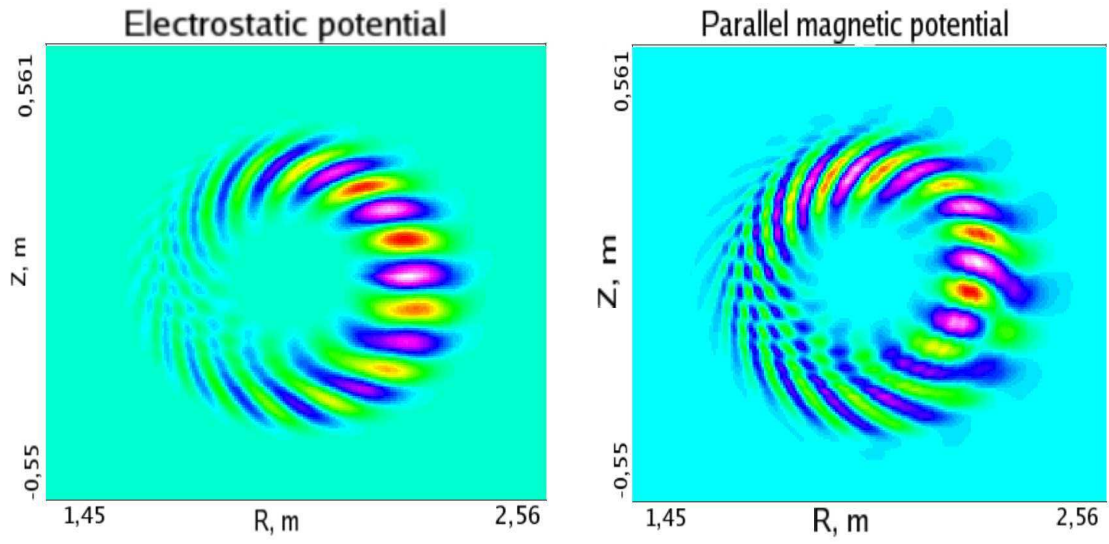
FIG. 12: (Color online): The structure of electrostatic and magnetic potentials (KBM instability) in the tokamak cross-section. Parameters as on Fig. 11 corresponding to the point with $\beta = 4\%$.

TABLE I: see parameters in the main text

$|C_k|$	ω_k	γ_k
13.2 %	0.44 MHz	-6.5 kHz
12.2 %	0.38 MHz	-50.9 kHz
11.4 %	0.5 MHz	-19.4 kHz
10.2 %	0.53 MHz	-63.9 kHz
8.4 %	0.419 MHz	-4.12 kHz

TABLE II: see parameters in the main text

$|C_k|$	ω_k	γ_k
26.4 %	0.44 MHz	-6.81 kHz
17.6 %	0.42 MHz	-4.24 kHz
10.4 %	0.51 MHz	-25.38 kHz
5.1 %	0.5 MHz	-11.92 kHz

TABLE III: see parameters in the main text

$|C_k|$	ω_k	γ_k
21 %	0.44 MHz	-6.3 kHz
15.5 %	0.4 MHz	-49.4 kHz
14.3 %	0.417 MHz	-4.3 kHz
6.7 %	0.513 MHz	-22.8 kHz